Effects of plasma medium and King dark matter halo surrounding black holes on weak gravitational lensing

Shokhzod Jumaniyozov[1,2†] Javlon Rayimbaev[3‡] Yassine Sekhmani[4,5,6§] Satimbay Palvanov[7ǂ]
Ahmadjon Abdujabbarov[8,9,10♯] Chengxun Yuan (袁承勋)[8¶]

[1]New Uzbekistan University, Tashkent 100000, Uzbekistan
[2]Tashkent State Technical University, Tashkent 100095, Uzbekistan
[3]Kimyo International University in Tashkent, Tashkent 100121, Uzbekistan
[4]Farabi University, Almaty 050040, Kazakhstan
[5]Center for Theoretical Physics, Khazar University, Baku AZ1096, Azerbaijan
[6]Centre for Research Impact & Outcome, Chitkara University Institute of Engineering and Technology, Chitkara University, Rajpura 140401, India
[7]National University of Uzbekistan, Tashkent 100174, Uzbekistan
[8]School of Physics, Harbin Institute of Technology, Harbin 150001, China
[9]University of Tashkent for Applied Sciences, Tashkent 100149, Uzbekistan
[10]Institute of Fundamental and Applied Research, National Research University TIIAME, Tashkent 100000, Uzbekistan

Abstract: This work examines how a Schwarzschild black hole embedded within a King dark matter halo and immersed in a dispersive, cold plasma leaves observable imprints on photon trajectories. For the King profile $(\mu,\nu,\alpha)=(3,2,0)$ we obtain a closed-form analytic metric that recovers the Schwarzschild solution once the dark matter contribution vanishes. Applying the Hamilton–Jacobi method to photon propagation in a plasma, we evaluate the photon-sphere radius and the black-hole shadow for both homogeneous and spatially varying plasma configurations. We find that plasma pushes the photon sphere to larger radii while simultaneously shrinking the shadow's apparent size relative to the vacuum case. Comparing these predictions with Event Horizon Telescope shadow measurements of M87* and Sgr A* yields only weak upper limits on the halo's central density and core radius, showing that physically realistic King halos remain consistent with the observed shadows. We further obtain analytic and semi-analytic deflection-angle and magnification formulas in the weak-lensing regime for three plasma configurations: uniform, singular isothermal sphere (SIS), and non-singular isothermal sphere (NSIS). Of these, the homogeneous plasma yields the largest enhancement of both the deflection angle and the magnification relative to vacuum, whereas the SIS profile, despite likewise enhancing the deflection, produces the smallest such enhancement of the models studied. These findings indicate that plasma contributions cannot be neglected when weak gravitational lensing is employed to constrain dark matter concentrations around supermassive black holes.

Keywords: King dark matter model, gravitational lensing, black holes, plasma medium

DOI: 10.1088/1674-1137/ae9fbe **CSTR:** 32044.14.ChinesePhysicsC.50115118

I. INTRODUCTION

Galactic centers are thought to host supermassive black holes (SMBHs) enveloped by considerable quantities of dark matter. ΛCDM-based numerical simulations of cosmic structure formation robustly predict dense spikes or extended dark-matter halos surrounding these central objects [1−3]. While the precise shape of such concentrations is still debated, observationally motivated forms such as the King profile [4, 5] are routinely adopted to characterize globular clusters and galactic nuclear star clusters. This profile offers an analytically tractable, physically sensible representation of a cored, finite-density dark-matter distribution free of unphysical divergences at the center.

Among the empirically motivated dark-matter density profiles available, the King profile brings several benefits to the present analysis: its central density stays fi-

Received 3 July 2026; Accepted 27 August 2026; Accepted manuscript online 28 August 2026
† E-mail: sh.jumaniyozov@newuu.uz
‡ E-mail: javlonrayimbaev6@gmail.com
§ E-mail: sekhmaniyassine@gmail.com
ǂ E-mail: satimbay@yandex.ru
♯ E-mail: ahmadjon@astrin.uz
¶ E-mail: yuancx@hit.edu.cn
©2026 Chinese Physical Society and the Institute of High Energy Physics of the Chinese Academy of Sciences and the Institute of Modern Physics of the Chinese Academy of Sciences and IOP Publishing Ltd. All rights, including for text and data mining, AI training, and similar technologies, are reserved.

nite, sidestepping the cuspy divergence typical of NFW- or Hernquist-type forms; the shape parameters chosen here lead to an exact, closed-form metric; and the profile itself originates from a physically grounded dynamical distribution function long used for globular clusters and galactic nuclear star clusters, settings that are dynamically comparable to the region immediately surrounding a supermassive black hole. Together, these features make the King profile a natural, analytically convenient tool for exploring how dark matter and plasma jointly influence the region near a black hole horizon.

At the same time, the region around an SMBH is far from an ideal vacuum. Accretion flows, hot coronae, and plasma in the broad-line region together form a dispersive, frequency-dependent medium capable of noticeably reshaping photon trajectories [6, 7]. Numerous studies confirm that even a fairly dilute plasma can appreciably change strong-field observables such as the black-hole shadow [8, 9], as well as weak-field lensing signatures [10]. Spatially varying plasma configurations, singular or non-singular isothermal spheres among them, are especially notable in this respect, since they can behave as effective anti-lenses that sharply reduce both the light-deflection angle and the resulting image magnification [11, 12].

Although dark-matter-modified spacetimes and plasma effects have each attracted considerable attention individually, a treatment that unifies the two has so far been missing. Closing this gap matters: the Event Horizon Telescope has already resolved the shadows of M87* [13] and Sgr A* [14] at unprecedented resolution, and forthcoming microlensing surveys (LSST, Roman Space Telescope) together with astrometric missions (Gaia, Theia) are poised to probe weak-lensing signals from intermediate-mass and supermassive black holes. Analyzing such data while ignoring either dark matter or plasma risks producing biased estimates of the black hole and halo parameters.

The literature on gravitational lensing and black-hole shadows under plasma has expanded considerably over the past several years. Yet, although prior work has carefully investigated how plasma affects a variety of modified black-hole spacetimes, no study to date has combined a black hole embedded in an observationally motivated, physically realistic dark-matter halo, such as the King profile, with a surrounding dispersive plasma. The resulting competition between the extra gravitational pull of the halo and the dispersive effects of the plasma has therefore not yet been examined.

Here we provide what is, to our knowledge, the first comprehensive treatment of weak gravitational lensing by a Schwarzschild black hole set within a King dark-matter halo and embedded in a cold, non-magnetized plasma. We construct an exact analytic metric for the specific King profile considered, one that reduces smoothly to the Schwarzschild geometry once the dark-matter contribution is switched off. Applying the Hamilton–Jacobi formalism appropriate to dispersive media, we obtain the photon sphere, black-hole shadow, deflection angle, and image magnification for both homogeneous and spatially non-uniform plasma. Confronting these predictions with current EHT shadow data for M87* and Sgr A*, we show that realistic King halos are fully consistent with the observations, while emphasizing that plasma effects must be modeled carefully to prevent misattributing future lensing signals to exotic physics.

The remainder of the paper proceeds as follows. Section II derives the exact spacetime metric. Photon spheres and shadows under plasma are analyzed in Secs. III and IV, while Sec. V presents the resulting EHT-based constraints. Weak gravitational lensing and image magnification for the different plasma profiles are treated in Secs. VI–VII, and Sec. VIII concludes the paper.

We adopt the $(-,+,+,+)$ metric signature and geometrized units ($G = c = 1$) throughout. Latin indices $(i, j, \ldots)$, ranging over 1 to 3, label spatial coordinates, while Greek indices $(\mu, \nu, \ldots)$, ranging over 0 to 3, label spacetime components.

II. SCHWARZSCHILD BH SURROUNDED BY KING DARK MATTER HALO

We consider a static, spherically symmetric spacetime that describes a Schwarzschild black hole embedded in an isotropic King dark-matter halo. In standard Schwarzschild-like coordinates, the line element reads [15]

$$\mathrm{d}s^2 = -f(r)\,\mathrm{d}t^2 + f(r)^{-1}\,\mathrm{d}r^2 + r^2\left(\mathrm{d}\theta^2 + \sin^2\theta\,\mathrm{d}\phi^2\right), \quad (1)$$

with

$$f(r) = 1 - \frac{2m(r)}{r}. \quad (2)$$

Here the lapse function $f(r)$ follows from solving the Einstein field equations [16],

$$R_{\mu\nu} - \frac{1}{2}R g_{\mu\nu} = 8\pi T_{\mu\nu}, \quad (3)$$

taken for an anisotropic fluid representing the King dark-matter distribution. Its energy–momentum tensor is diagonal, $T_{\mu\nu} = \mathrm{diag}\left(-\rho(r),\, \tilde{\tau}(r),\, p(r),\, p(r)\right)$, with $\rho(r)$ the energy density, $\tilde{\tau}(r)$ the radial pressure, and $p(r)$ the tangential pressure. Integrating the structure equations for a static, spherically symmetric anisotropic fluid directly gives [17, 18]

$$\rho(r) = -\tilde{\tau}(r) = \frac{1}{4\pi r^2}\frac{\mathrm{d}m(r)}{\mathrm{d}r}, \tag{4}$$

$$p(r) = -\frac{1}{8\pi r}\frac{\mathrm{d}^2 m(r)}{\mathrm{d}r^2}, \tag{5}$$

with $m(r)$ the mass function, i.e., the gravitational mass contained within a sphere of radius r. We take the density to follow the three-parameter Dekel–Zhao profile

$$\rho(r) = \rho_s \left(\frac{r}{r_s}\right)^{\mu-3}\left[1+\left(\frac{r}{r_s}\right)^{\nu}\right]^{-(\mu+\alpha)/\nu} \tag{6}$$

with central density ρ_s, scale radius r_s, and dimensionless shape parameters (μ,ν,α). Setting $(\mu,\nu,\alpha)=(3,2,0)$ recovers the King dark-matter profile, giving the compact analytic form

$$\rho(r) = \rho_s \left(1+\frac{r^2}{r_s^2}\right)^{-3/2}. \tag{7}$$

This form coincides with the β-model at $\beta = 1$, which describes observed galactic and cluster dark-matter halos remarkably well while remaining fully tractable analytically. Inserting Eq. (7) into the Einstein equations and integrating produces the exact lapse function [19]:

$$f(r) = 1 - \frac{2M}{r} + \frac{8\pi\rho_s r_s^3}{\sqrt{r^2+r_s^2}} + \frac{8\pi\rho_s r_s^3}{r}\ln\left(\frac{\sqrt{r^2+r_s^2}-r}{r_s}\right). \tag{8}$$

It is worth stressing that r_s here refers to the scale radius of a compact, nuclear dark-matter concentration gravitationally bound to the black hole, rather than the radius of the extended, galactic-scale halo. For M87* and Sgr A*, $r_s/M \sim O(1)$ corresponds to physical scales of roughly 10^{-4}–10^{-2} pc, comfortably inside the black hole's sphere of influence. If instead one adopts galactic-scale core radii ($r_s/M \gtrsim 10^6$), the King density becomes essentially uniform across the photon-sphere region, making it indistinguishable from a constant dark-matter background in the shadow and lensing observables studied here. Taking either $\rho_s \to 0$ or $r_s \to 0$ reduces the metric of Eqs. (1)–(8) smoothly to the vacuum Schwarzschild solution. We define the event-horizon radius r_h as the largest root of $f(r_h) = 0$.

Figure 1 traces the event-horizon radius r_h/M as the King halo parameters vary. The left panel plots r_h/M against the core radius r_s/M for several values of the central density $\rho_s M^2$, and the right panel plots it against $\rho_s M^2$ for several values of r_s/M. Both parameters push r_h/M upward: increasing the central density $\rho_s M^2$ substantially enlarges the horizon, and increasing the core radius r_s/M likewise increases r_h/M.

III. PHOTON MOTION IN THE PRESENCE OF PLASMA

To study weak gravitational lensing by a BH surrounded by a King dark-matter halo and an unmagnetized, homogeneous plasma, we employ the Hamilton–Jacobi approach suited to dispersive media. In a cold plasma the dispersion relation reshapes the effective geometry seen by photons, and the Hamiltonian governing null rays in such a medium takes the form [20–24]

$$\tilde{H}(x^\alpha, p_\beta) = \frac{1}{2}\tilde{g}^{\alpha\beta}p_\alpha p_\beta = 0, \tag{9}$$

where the effective (optical) metric is

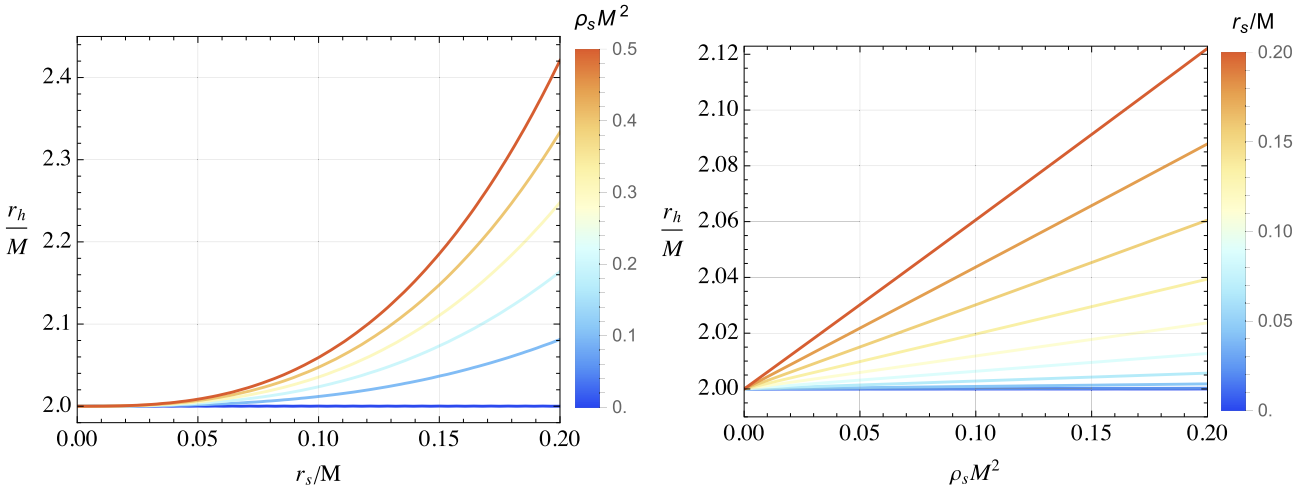


Fig. 1. (color online) How the event-horizon radius r_h of the BH changes with the central density parameter ρ_s and the core radius parameter r_s.

$$\tilde{g}^{\alpha\beta} = g^{\alpha\beta} + (1-n^2)u^\alpha u^\beta. \tag{10}$$

Here n is the plasma refractive index, and $u^a = (1,0,0,0)$ denotes the four-velocity of a static observer in the coordinates of Eq. (1).

For a cold, unmagnetized plasma the refractive index reads [25–27]

$$n^2(r) = 1 - \frac{\omega_p^2(r)}{\omega_0^2(r)}. \tag{11}$$

Here $\omega_p^2 = e^2 N_e/(\pi m_e)$ is the squared plasma frequency, with e and m_e the electron charge and mass and N_e the electron number density, while $\omega(r)$ denotes the photon's angular frequency as measured by a static observer:

$$\omega(r) = \frac{\omega_0}{\sqrt{f(r)}}. \tag{12}$$

The constant $\omega_0 = -p_t = E$ represents the photon's conserved energy at spatial infinity, where $f(\infty) = 1$, and photons can only propagate where $\omega(r) > \omega_p$, that is, $\omega_p/\omega_0 < 1$.

Restricting motion to the equatorial plane ($\theta = \pi/2$, $p_\theta = 0$), the conserved energy $E = -p_t$ and angular momentum $L = p_\phi$ produce the normalized photon four-velocity components [28–31]:

$$\begin{aligned} \dot{t} &\equiv \frac{\mathrm{d}t}{\mathrm{d}\lambda} = \frac{-p_t}{f(r)}, \\ \dot{r} &\equiv \frac{\mathrm{d}r}{\mathrm{d}\lambda} = p_r f(r), \\ \dot{\phi} &\equiv \frac{\mathrm{d}\phi}{\mathrm{d}\lambda} = \frac{p_\phi}{r^2}. \end{aligned} \tag{13}$$

Combining these relations gives the trajectory equation for the photon's path

$$\frac{\mathrm{d}r}{\mathrm{d}\phi} = \frac{\dot{r}}{\dot{\phi}} = \frac{f(r) r^2 p_r}{p_\phi}. \tag{14}$$

Imposing the null condition $H = 0$ on the photon motion then leads to

$$\frac{\mathrm{d}r}{\mathrm{d}\phi} = \pm r\sqrt{f(r)}\sqrt{h^2(r)\frac{\omega_0^2}{p_\phi^2} - 1}, \tag{15}$$

where we define

$$h^2(r) \equiv r^2\left[\frac{1}{f(r)} - \frac{\omega_p^2(r)}{\omega_0^2}\right]. \tag{16}$$

As usual, the photon-sphere radius $r_{\rm ph}$ in the plasma follows from requiring an extremum of the effective potential [32–34]:

$$\frac{\mathrm{d}}{\mathrm{d}r}\left(h^2(r)\right)\Big|_{r=r_{\rm ph}} = 0. \tag{17}$$

Combining Eqs. (16) and (17) yields the following expression governing the photon-sphere radius $r_{\rm ph}$ in the plasma:

$$\begin{aligned} &\frac{2r_{\rm ph}\left(4\pi r_s^3\rho_s\left(\frac{r_{\rm ph}r_s^2}{\left(r_{\rm ph}^2+r_s^2\right)^{3/2}} + \ln\left(\frac{\sqrt{r_{\rm ph}^2+r_s^2}-r_{\rm ph}}{r_s}\right)\right)-1\right)}{\left(r_{\rm ph}\left(\frac{8\pi r_s^3\rho_s}{\sqrt{r_{\rm ph}^2+r_s^2}}-1\right) - 8\pi r_s^3\rho_s\ln\left(\frac{\sqrt{r_{\rm ph}^2+r_s^2}-r_{\rm ph}}{r_s}\right)+2\right)^2} \\ &- \frac{2r_{\rm ph}}{r_{\rm ph}\left(\frac{8\pi r_s^3\rho_s}{\sqrt{r_{\rm ph}^2+r_s^2}}-1\right) - 8\pi r_s^3\rho_s\ln\left(\frac{\sqrt{r_{\rm ph}^2+r_s^2}-r_{\rm ph}}{r_s}\right)+2} \\ &- \frac{2\omega_p^2}{\omega_0^2} = 0. \end{aligned} \tag{18}$$

A. Homegeneous plasma

For the particular case of a homogeneous plasma, where $\omega_p^2(r) = \text{const}$, we solve Eq. (18) for the photon-sphere radius numerically [35, 36].

Figure 2 presents these results, where r_{ph}/M grows monotonically with the plasma-frequency ratio ω_p^2/ω_0^2. A larger central dark-matter density ρ_s pushes the photon sphere farther out, while a larger core radius r_s/M produces a comparatively modest increase. Overall, a homogeneous plasma enlarges the photon sphere relative to vacuum.

B. Inhomogeneous plasma

Here we turn to photon spheres under a spatially nonuniform plasma whose frequency follows a simple power law [37]:

$$\omega_p^2 = \frac{z_0}{r^q}, \tag{19}$$

with z_0 and $q > 0$ free positive constants. To bring out the essential features of this power-law model, we focus on the case $q = 1$ with z_0 held fixed, a choice that exactly reproduces the diverging-lens behavior of a negative-mass Schwarzschild BH. Combining Eq. (19) with the general condition (18), we solve numerically for the photon-sphere radius in this inhomogeneous plasma. Figure 3 plots $r_{\rm ph}$ for the power-law plasma $\omega_p^2 = z_0/r^q$ against the

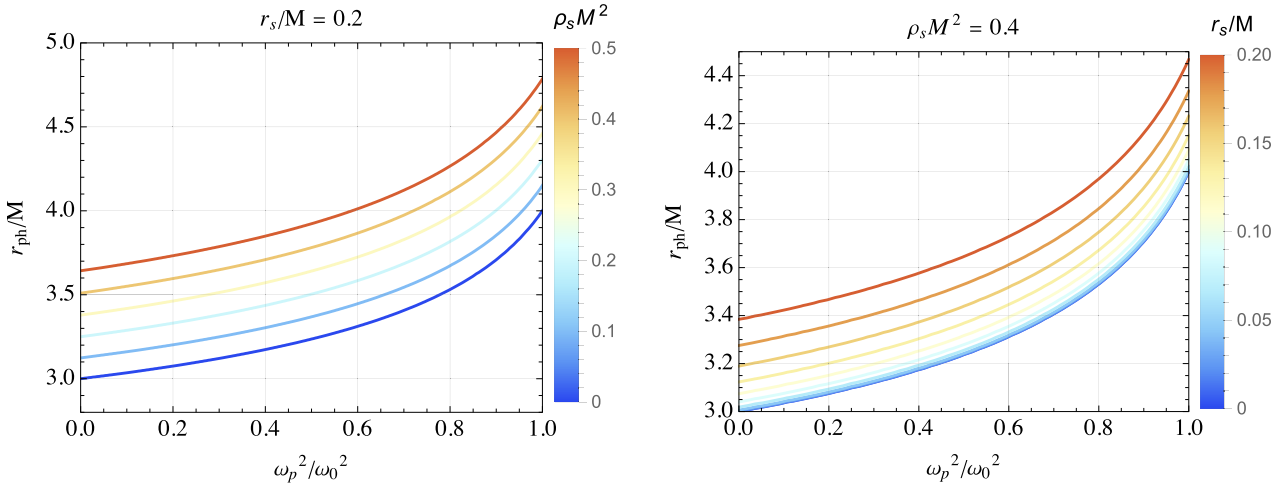


Fig. 2. (color online) Photon-sphere radius $r_{\rm ph}$ versus the homogeneous plasma frequency, shown for varying ρ_s (left) and r_s (right).

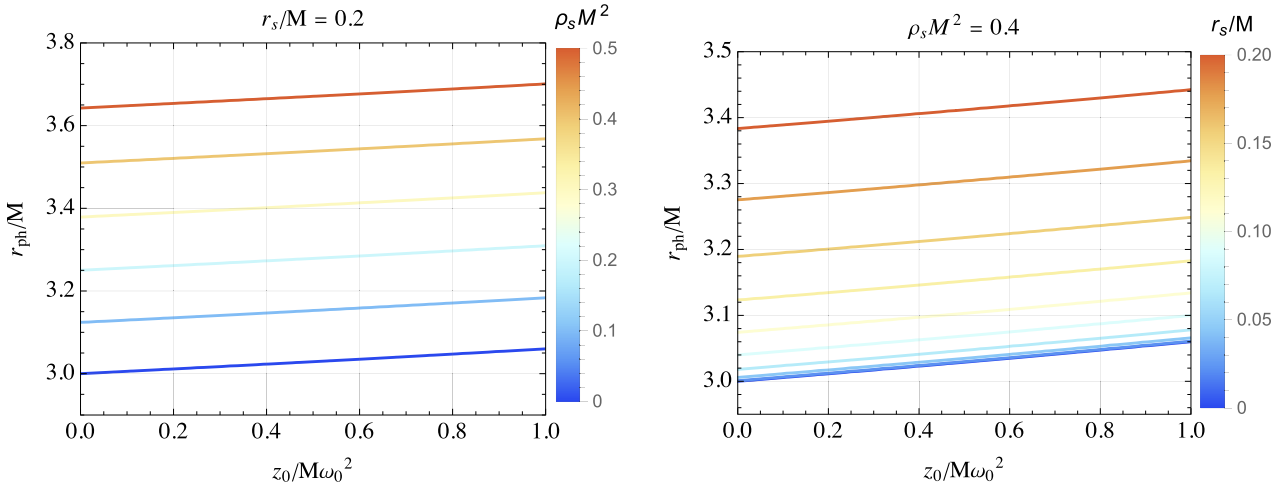


Fig. 3. (color online) Photon-sphere radius $r_{\rm ph}$ as a function of ρ_s (left) and r_s (right) for the power-law case $\omega_p^2 = z_0/r$.

dark-matter parameters. The photon-sphere radius keeps growing with the density parameter $\rho_s M^2$ and rises only slightly with core radius r_s/M. Relative to the homogeneous case, this particular non-uniform distribution has a weaker effect, so much so that the two plasma models are almost indistinguishable in terms of $r_{\rm ph}$.

IV. SHADOW OF A BH SURROUNDED BY PLASMA MEDIUM

We now turn to the shadow cast by a BH embedded in a dark-matter halo and viewed through the surrounding plasma. Geometrically, the shadow's angular radius $\alpha_{\rm sh}$ is given by [38–43]

$$\sin^2\alpha_{\rm sh} = \frac{h^2(r_p)}{h^2(r_0)} = \frac{r_p^2\left[\dfrac{1}{f(r_p)} - \dfrac{\omega_p^2(r_p)}{\omega_0^2}\right]}{r_0^2\left[\dfrac{1}{f(r_0)} - \dfrac{\omega_p^2(r_0)}{\omega_0^2}\right]}, \tag{20}$$

with r_p the photon-sphere radius and r_0 the radial coordinate of a distant observer.

For an observer sufficiently far from the black hole ($r_0 \to \infty$), $h(r) \to r$, and this asymptotic limit lets the observed shadow radius be approximated as [44–47]

$$R_{\rm sh} \approx r_0 \sin\alpha_{\rm sh} = \sqrt{r_p^2\left(\frac{1}{f(r_p)} - \frac{\omega_p^2(r_p)}{\omega_0^2}\right)}. \tag{21}$$

Setting $\omega_p(r) \equiv 0$ removes the plasma correction and recovers the familiar Schwarzschild shadow radius $R_{\rm sh} = 3\sqrt{3}M$, consistent with a photon sphere located at $r_{\rm ph} = 3M$.

Figures 4 and 5 give $R_{\rm sh}/M$ for a BH surrounded by a King halo under homogeneous and inhomogeneous plasma, respectively. In each case the shadow shrinks as the plasma frequency rises. A larger central density $\rho_s M^2$ enlarges the shadow, and a larger core radius r_s/M similarly tends to increase $R_{\rm sh}/M$. On the whole, plasma re-

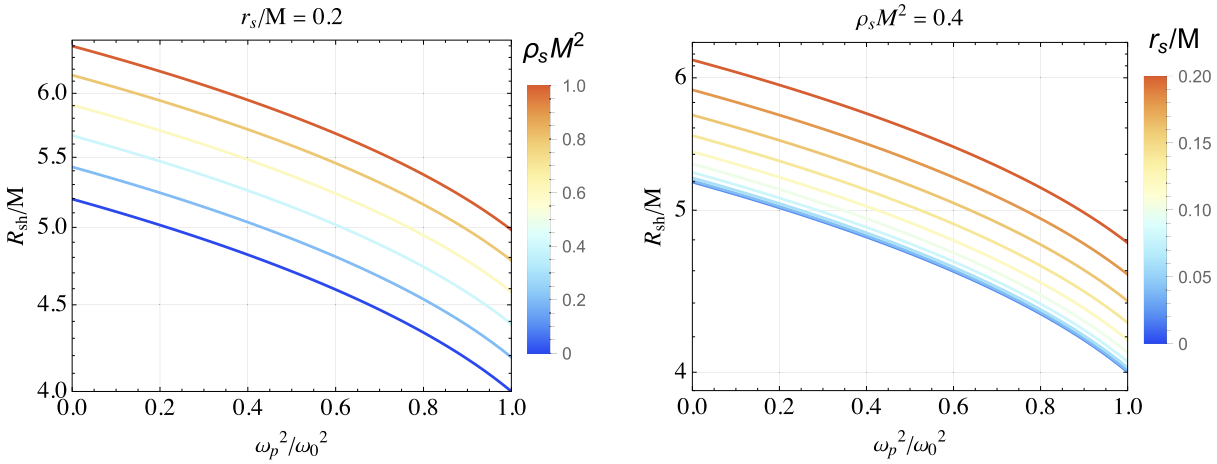


Fig. 4. (color online) BH shadow radius R_{sh} versus the homogeneous plasma frequency, for varying ρ_s (left) and r_s (right).

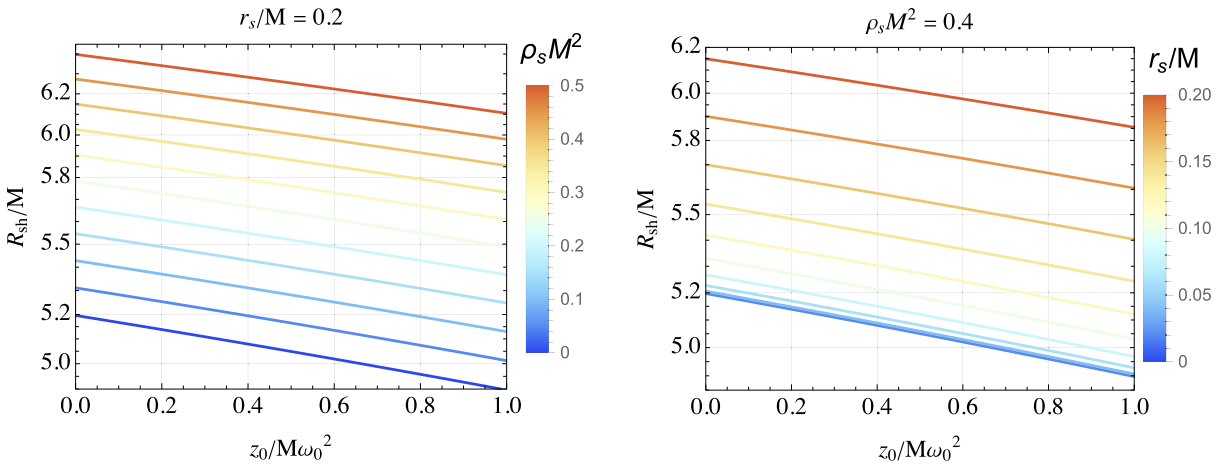


Fig. 5. (color online) BH shadow radius R_{sh} as a function of ρ_s (left) and r_s (right) for the power-law case $\omega_p^2 = z_0/r$.

duces the observed shadow relative to vacuum.

V. CONSTRAINTS FROM EHT OBSERVATIONS

We confront our model with real astrophysical data by using the most recent EHT Collaboration measurements of the shadow angular diameters for M87* and Sgr A*. Following the usual procedure [48, 49], the measured angular diameter θ_{sh} connects to the theoretical shadow radius R_{sh} through

$$\theta_{sh} = 2\frac{R_{sh}}{D}, \tag{22}$$

with D the Earth–BH distance.

For M87*, we use the values from [13]:

$$\begin{aligned} \theta_{sh}^{M87*} &= 42 \pm 3\,\mu\text{as}, \\ D_{M87*} &= 16.8 \pm 0.8\,\text{Mpc}, \\ M_{M87*} &= (6.5 \pm 0.7) \times 10^9 M_\odot. \end{aligned} \tag{23}$$

The corresponding EHT and complementary values for Sgr A* are taken from [14]:

$$\begin{aligned} \theta_{sh}^{SgrA*} &= 48.7 \pm 7\,\mu\text{as}, \\ D_{SgrA*} &= 8277 \pm 9\,\text{pc}, \\ M_{SgrA*} &= (4.297 \pm 0.013) \times 10^6 M_\odot. \end{aligned} \tag{24}$$

With the theoretical shadow-radius expression R_{sh}/M from the previous sections, we invert $\theta_{sh} = 2R_{sh}/D$ for the King halo parameters $(\rho_s M^2, r_s/M)$, for both the homogeneous plasma of Sec. III.A and the power-law model $\omega_p^2 = z_0/r$ of Sec. III.B. Figures 6 and 7 present the results. In each figure, the left panels vary the central density $\rho_s M^2$ at fixed core radius $r_s/M = 0.2$, and the right panels vary the core radius r_s/M at fixed $\rho_s M^2 = 0.4$. Thick black curves mark the central observed values of θ_{sh}, with shaded bands indicating the 1σ uncertainty.

Comparing the two cases, plasma, whether homogeneous or inhomogeneous, shifts the allowed region toward

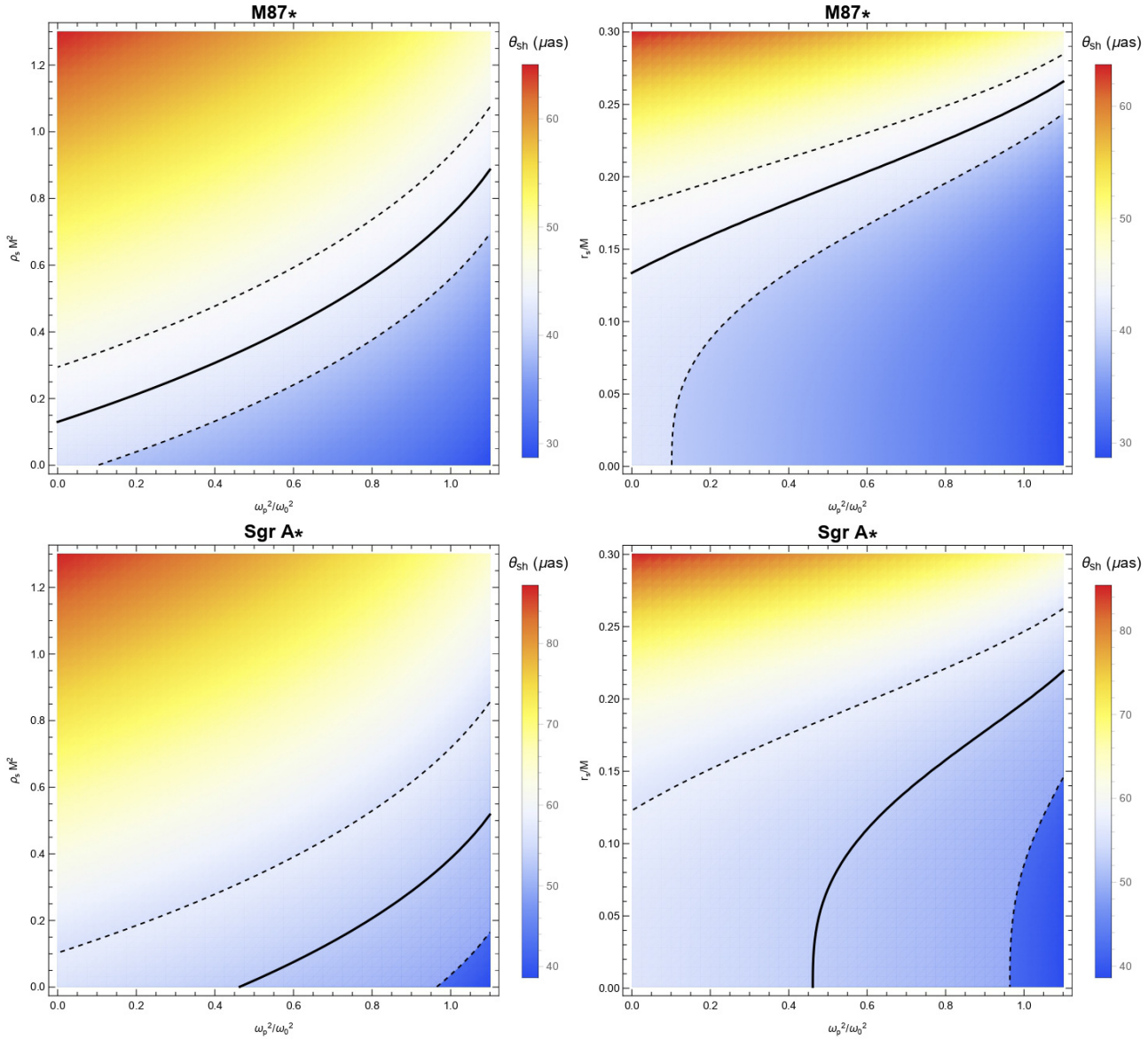


Fig. 6. (color online) How the dark-matter parameters ρ_s (left panels) and r_s (right panels) relate to the plasma parameter, inferred from the measured shadow angular diameters of M87* (top) and Sgr A* (bottom). Black curves mark the central shadow diameters $\theta_{sh} = 39\mu$as (M87*) and $\theta_{sh} = 41.7\mu$as (Sgr A*); shaded bands show the 1σ regions obtained by propagating the measurement uncertainty in θ_{sh}, so that any $(\rho_s M^2, r_s/M)$ pair inside a band is consistent with the EHT data at 1σ.

somewhat higher central densities $\rho_s M^2$ than in vacuum. The allowed regions for the two plasma models are qualitatively alike and shift only marginally relative to each other (compare Fig. 7 with Fig. 6), implying that the EHT constraint on the King halo is not very sensitive to the assumed plasma distribution, and that the plasma parameter itself (ω_p^2/ω_0^2 in the homogeneous case, z_0 in the inhomogeneous case) is pinned down to a similar degree in both scenarios. Even so, a broad swath of realistic King halo parameters ($\rho_s M^2 \lesssim 0.5$, $r_s/M \gtrsim 0.1$) stays fully consistent with the current EHT data for M87* and Sgr A*, regardless of which plasma model is assumed. Indeed, fairly dense halos with $\rho_s M^2 \approx 0.5$ and moderate core radii $r_s/M \approx 0.2$ remain compatible with the observed shadow sizes under both plasma scenarios.

The current EHT shadow data therefore neither rule out a King dark-matter halo around these SMBHs nor impose more than mild upper limits on the central density nearby, essentially independent of whether the plasma is modeled as homogeneous or inhomogeneous. Higher-precision EHT measurements in the future ($\sim 1\mu$as resolution) should meaningfully tighten these bounds and could eventually separate vacuum from plasma-affected cases, and perhaps distinguish between the plasma distributions

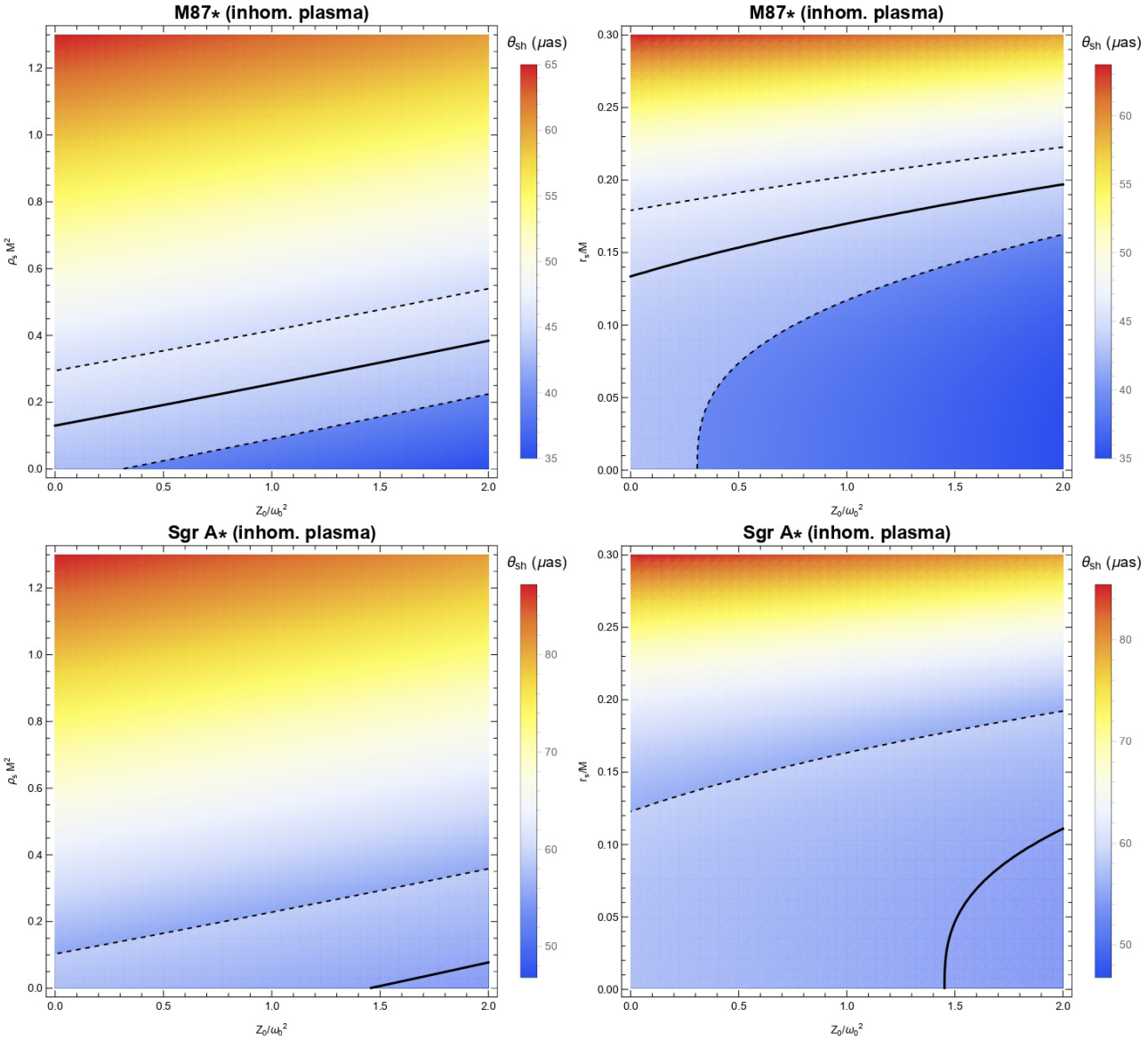


Fig. 7. (color online) Corresponding 1σ-allowed regions for the inhomogeneous power-law plasma model of Eq. (19).

themselves.

VI. GRAVITATIONAL WEAK LENSING IN PRESENCE OF THE PLASMA MEDIUM

This section examines the gravitational deflection of light by a Schwarzschild BH surrounded by a dark-matter halo and plasma, working within the weak-field approximation. The spacetime metric takes the form [50–53]

$$g_{\alpha\beta} = \eta_{\alpha\beta} + h_{\alpha\beta}, \tag{25}$$

with $\eta_{\alpha\beta} = \mathrm{diag}(-1,1,1,1)$ the Minkowski metric, $|h_{\alpha\beta}| \ll 1$, and $h_{\alpha\beta} \to 0$ as $r \to \infty$. To linear order the inverse metric reads

$$g^{\alpha\beta} = \eta^{\alpha\beta} - h^{\alpha\beta}, \quad \text{with} \quad h^{\alpha\beta} = h_{\alpha\beta}. \tag{26}$$

We next work out the deflection angle for photons traveling through this plasma. For a cold plasma with electron plasma frequency ω_e and observed photon frequency ω, the deflection along direction i is [54–57]

$$\hat{\alpha}_i = \pm\frac{1}{2}\int_{-\infty}^{\infty}\left[\frac{1}{2}\left(h_{33,i} + \frac{\omega_0^2}{\omega_0^2-\omega_e^2}h_{00,i}\right) - \frac{K_e\,\omega_0^2}{\omega_0^2-\omega_e^2}N_{,i}\right]\mathrm{d}z, \tag{27}$$

with $N(\mathbf{x})$ the electron number density, $K_e = 4\pi e^2/m_e$, and the $\pm$ sign denoting deflection toward or away from the

lens.

Far from the source, the perturbed line element takes the approximate Newtonian form [58, 59]

$$\mathrm{d}s^2 = \mathrm{d}s_0^2 + h_{tt}\,\mathrm{d}t^2 + h_{rr}\,\mathrm{d}r^2. \tag{28}$$

Here $\mathrm{d}s_0^2 \equiv \eta_{\alpha\beta}\mathrm{d}x^\alpha \mathrm{d}x^\beta = -\mathrm{d}t^2 + \mathrm{d}r^2 + r^2(\mathrm{d}\theta^2 + \sin^2\theta\,\mathrm{d}\phi^2)$ denotes the flat background appearing in the split $g_{\alpha\beta} = \eta_{\alpha\beta} + h_{\alpha\beta}$; h_{tt} and h_{rr} are the linear-order corrections sourced by the black hole mass and King halo, written explicitly below via h_{00} and $h_{jk} = h_{00}n_j n_k$; and $R_s = 2M$ is the Schwarzschild radius. Working in Cartesian coordinates along the photon path, with impact parameter b and propagation direction z, the nonzero perturbation components sourced by the black hole and the dark-matter halo are

$$h_{00} = \frac{R_s}{r} + \frac{8\pi\rho_s r_s^3}{\sqrt{r^2+r_s^2}} - \frac{8\pi\rho_s r_s^3}{r}\ln\left(\frac{\sqrt{r^2+r_s^2}-r}{r_s}\right), \tag{29}$$

$$h_{jk} = h_{00}\,n_j n_k, \tag{30}$$

$$h_{33} = h_{00}\cos^2\chi, \tag{31}$$

with $r = \sqrt{b^2+z^2}$, $\cos\chi = z/r$, and n_j the unit radial vector projected onto the spatial indices.

We now examine how both uniform and non-uniform plasma distributions influence the resulting deflection angle.

A. Uniform plasma

We first take a homogeneous plasma, $\omega_0^2 = \text{const}$, for which the refractive index carries no explicit spatial dependence, so the refractive term in Eq. (27) can be dropped. Integrating Eq. (27) under this simplification gives the deflection angle [12]:

$$\begin{aligned}\hat{\alpha}_{\text{uni}} = \frac{1}{b\left(b^2+r_s^2\right)}\Bigg(2\Bigg(b^2\left(4\pi r_s^3\rho_s\left(\frac{\omega_p^2}{\omega_0^2}+1\right)+\frac{\omega_p^2}{\omega_0^2}+2\right)\\ +2\pi r_s^2\rho_s\left(b^2+r_s^2\right)\Bigg(\left(\frac{\omega_p^2}{\omega_0^2}+2\right)r_s\ln\left(\frac{b^2+r_s^2}{r_s^2}\right)\\ +4b\tan^{-1}\left(\frac{r_s}{b}\right)\Bigg)+\left(\frac{\omega_p^2}{\omega_0^2}+2\right)r_s^2\Bigg)\Bigg).\end{aligned} \tag{32}$$

Figure 8 plots $\hat{\alpha}_{\text{uni}}$ against b/M for a uniform plasma, at several values of ω_p^2/ω_0^2, $\rho_s M^2$, and r_s/M. The trend matches expectations: at fixed dark-matter parameters, the deflection angle grows with ω_p^2/ω_0^2. A denser central concentration (larger $\rho_s M^2$) enhances the bending, and an even stronger enhancement follows from a larger core radius r_s/M. In every case the uniform plasma boosts the deflection well above the vacuum value ($\omega_p^2 = 0$), most markedly at large impact parameters.

B. Singular isothermal sphere

The singular isothermal sphere (SIS) is commonly treated as the simplest and most instructive model for capturing the essential features of strongly lensed photons. Originally proposed to describe large-scale density profiles of galaxies and galaxy clusters, it consists of a spherically symmetric gas cloud whose density diverges at the center. Its mass-density profile is [60, 61]

$$\rho(r) = \frac{\sigma_v^2}{2\pi r^2}, \tag{33}$$

where σ_v is the one-dimensional velocity dispersion. The corresponding plasma number density (equivalently, the electron column density along the line of sight) is then

$$N(r) = \frac{\rho(r)}{\kappa m_p} = \frac{\sigma_v^2}{2\pi\kappa m_p r^2}, \tag{34}$$

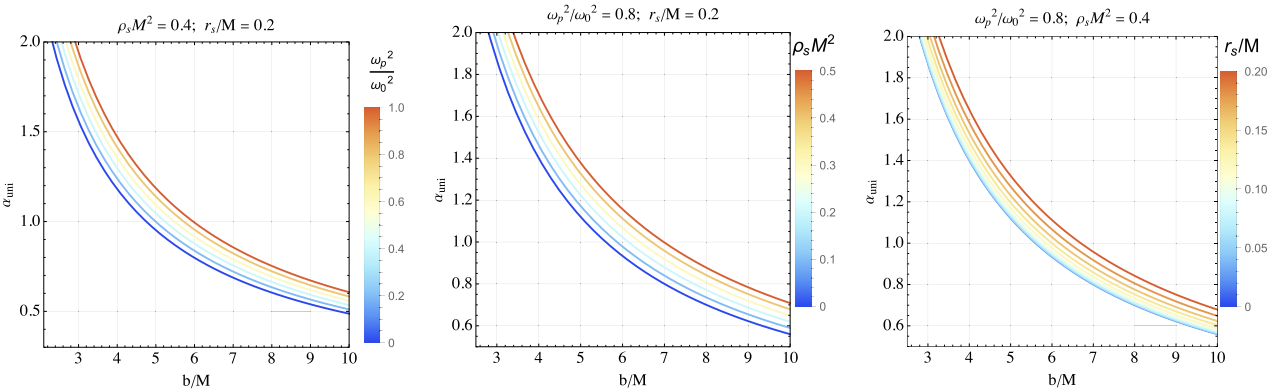


Fig. 8. (color online) Deflection angle α_{uni} versus impact parameter b, for various values of the plasma parameter ω_p^2/ω_0^2 and the dark-matter parameters ρ_s and r_s.

with m_p the proton mass and κ a dimensionless constant tied to the ionization fraction and dark-matter-dominated cosmology. The squared plasma frequency associated with this electron density then takes the analytic form

$$\omega_e^2(r) = K_e N(r) = \frac{K_e \sigma_v^2}{2\pi\kappa m_p r^2}, \tag{35}$$

with $K_e = 4\pi e^2/m_e$ the standard plasma-frequency constant. Using these SIS properties, the plasma-modified deflection angle $\hat{\alpha}_{\rm SIS}$ is

$$\begin{aligned}\hat{\alpha}_{\rm SIS} =& \frac{1}{3b^3}\left(16b^3\rho_s \tan^{-1}\left(\frac{r_s}{b}\right)\left(\frac{8\omega_c^2}{\omega_0^2}+3\pi r_s^2\right)\right.\\ &+8r_s^3\rho_s\left(3\pi b^2+\frac{4\omega_c^2}{\omega_0^2}\right)\ln\left(\frac{b^2+r_s^2}{r_s^2}\right)+12b^2-\frac{6b\omega_c^2}{\omega_0^2}\\ &\left.+\frac{16\omega_c^2}{\pi\omega_0^2}-\frac{8b^2 r_s\rho_s\left(\frac{4\omega_c^2\left(4b^2+r_s^2\right)}{\omega_0^2}-3\pi b^2 r_s^2\right)}{b^2+r_s^2}\right),\end{aligned}$$

with the auxiliary plasma-frequency scale ω_c^2 defined as

$$\omega_c^2 \equiv \frac{\sigma_v^2 K_e}{2\kappa m_p R_s^2}. \tag{36}$$

Figure 9 illustrates how the SIS plasma affects the deflection. Qualitatively the dependence on plasma strength and dark-matter parameters resembles the uniform-plasma case, though the effect is considerably smaller in magnitude. For fixed dark-matter parameters, $\hat{\alpha}_{\rm SIS}$ decreases as ω_c^2/ω_0^2 grows, staying above the vacuum value $\hat{\alpha}_{\rm vac}$ throughout; the enhancement it provides is consistently weaker than the uniform plasma's at matching parameter values, so $\hat{\alpha}_{\rm SIS}$ stays below $\hat{\alpha}_{\rm uni}$ over the entire range considered. As with the uniform case, the deflection angle also rises with both the central density $\rho_s M^2$ and the core radius r_s/M.

C. Non-singular isothermal sphere

We turn next to photon propagation through a non-singular isothermal sphere (NSIS), a more physically realistic description than the singular case, in which the central density singularity is regularized by introducing a finite core radius r_c. The mass-density profile then reads [10]

$$\rho(r) = \frac{\sigma_v^2}{2\pi(r^2+r_c^2)} = \frac{\rho_0}{1+\dfrac{r^2}{r_c^2}}, \qquad \rho_0 = \frac{\sigma_v^2}{2\pi r_c^2}, \tag{37}$$

with σ_v the one-dimensional velocity dispersion and ρ_0 the central density. The associated plasma (electron) number density for the NSIS model is

$$N(r) = \frac{\rho(r)}{\kappa m_p} = \frac{\sigma_v^2}{2\pi\kappa m_p(r^2+r_c^2)}, \tag{38}$$

with m_p the proton mass and κ a dimensionless ionization factor. The corresponding squared plasma frequency is then

$$\omega_e^2(r) = K_e N(r) = \frac{K_e\sigma_v^2}{2\pi\kappa m_p(r^2+r_c^2)}, \tag{39}$$

Integrating the ray equation analytically for this distribution gives the NSIS deflection angle [62]

$$\begin{aligned}\hat{\alpha}_{\rm NSIS} =& \frac{1}{b\left(b^2+9\right)}\left(\frac{8b^2 r_s^3\rho_s\left(\pi\left(b^2+9\right)+\dfrac{4\omega_c^2}{\omega_0^2}\right)}{b^2+r_s^2}\right.\\ &+8r_s^2\rho_s\left(4r_s\left(\pi\left(b^2+9\right)+\frac{2\omega_c^2}{\omega_0^2}\right)\ln\left(\frac{b^2+r_s^2}{r_s^2}\right)\right.\\ &\left.\left.+2\pi b\left(b^2+9\right)\tan^{-1}\left(\frac{r_s}{b}\right)\right)+4b^2+\frac{8\omega_c^2}{\pi\omega_0^2}+36\right).\end{aligned} \tag{40}$$

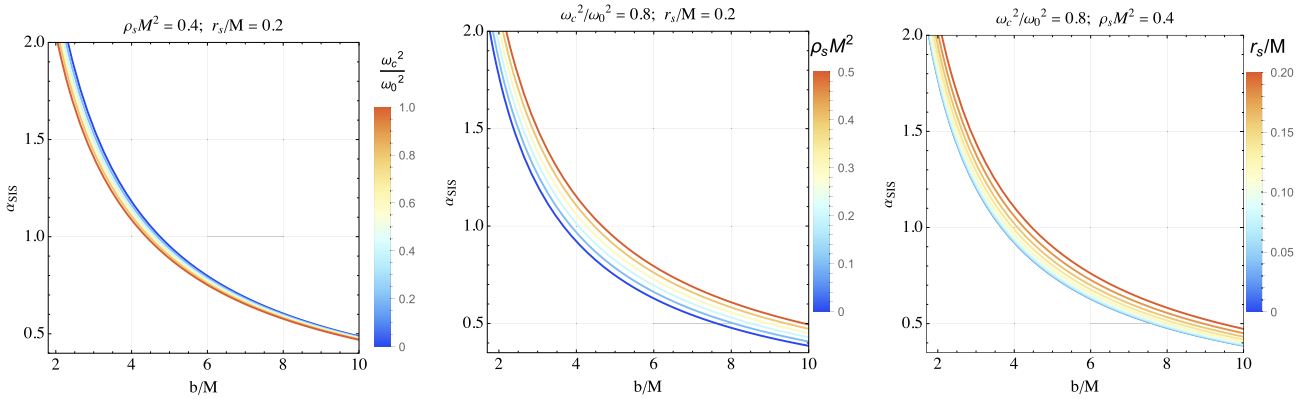


Fig. 9. (color online) Variation of $\alpha_{\rm SIS}$ with b, for different values of the plasma parameter ω_c^2/ω_0^2 and the dark-matter parameters ρ_s and r_s.

As before, we study $\hat{\alpha}_{\rm NSIS}$ both numerically and graphically, reporting all results via the dimensionless plasma parameter ω_c^2/ω^2, with ω_c^2 the characteristic plasma-frequency scale introduced earlier.

Figure 10 gives the analogous results for the more realistic NSIS model across a range of plasma and dark-matter parameters. The qualitative trends persist, with the suppression effect falling between the uniform and SIS cases.

Figure 11 then compares $\hat{\alpha}_{\rm vac}$, $\hat{\alpha}_{\rm uni}$, $\hat{\alpha}_{\rm SIS}$, and $\hat{\alpha}_{\rm NSIS}$ directly as functions of b:

$$\hat{\alpha}_{\rm uni} > \hat{\alpha}_{\rm NSIS} > \hat{\alpha}_{\rm SIS} > \hat{\alpha}_{\rm vac}, \tag{41}$$

These results confirm that, while all three plasma models enhance light bending beyond the vacuum value, the homogeneous plasma provides the largest boost, and the inhomogeneous models are comparatively less effective. Of the three, the SIS profile gives the weakest enhancement, with the NSIS profile falling in between the uniform and SIS cases.

The King halo's own contribution is examined separately in the middle and right panels of Figures 8, 9, and 10. A higher central density $\rho_s M^2$ consistently raises the deflection angle across all plasma configurations, and a larger core radius r_s/M produces a moderate increase in $\hat{\alpha}$ as well. Consequently, a substantial dark-matter concentration near the BH remains detectable through its weak-lensing signature even in the presence of a dispersive plasma.

VII. MAGNIFICATION OF GRAVITATIONALLY LENSED IMAGE

We now turn to how plasma affects the apparent brightness of the source, using the deflection angle $\hat{\alpha}$ obtained earlier for both the uniform-plasma and SIS environments.

Figure 12 sketches the standard lensing geometry, with the BH acting as lens for a distant background star. The lens equation linking the observed image position θ to the true source position β reads [63, 64]

$$\theta D_s = \beta D_s + \hat{\alpha} D_{ds}. \tag{42}$$

Introducing the impact parameter $b = D_d\theta$ and the auxiliary function $\xi(\theta) \equiv |\hat{\alpha}_b| b$ recasts Eq. (42) as

$$\beta = \theta - \frac{D_{ds}}{D_s}\frac{\xi(\theta)}{\theta D_d}. \tag{43}$$

Perfect alignment of source, lens, and observer ($\beta = 0$) produces, by axial symmetry, an Einstein ring of angular radius θ_0; for a Schwarzschild BH in vacuum this angle is

$$\theta_0 = \sqrt{2R_s\frac{D_{ds}}{D_d D_s}}, \tag{44}$$

where $R_S = 2M$ is the Schwarzschild radius.

Gravitational lensing manifests observationally as a shift in the source's apparent brightness. The total magnification μ_Σ of a point source sums over all images labeled by k:

$$\mu_\Sigma = \frac{I_{\rm tot}}{I_*} = \sum_k \left|\frac{\theta_k}{\beta}\frac{{\rm d}\theta_k}{{\rm d}\beta}\right|, \qquad k = 1, 2, \cdots, j, \tag{45}$$

with I_* the unlensed flux and j the number of images.

For a point-mass (or Schwarzschild) lens immersed in *uniform* plasma, well-known closed-form expressions are available for analytical work. With the dimensionless source position $x \equiv \beta/\theta_0$, the primary (positive-parity) and secondary (negative-parity) image magnifications in uniform plasma are [65]

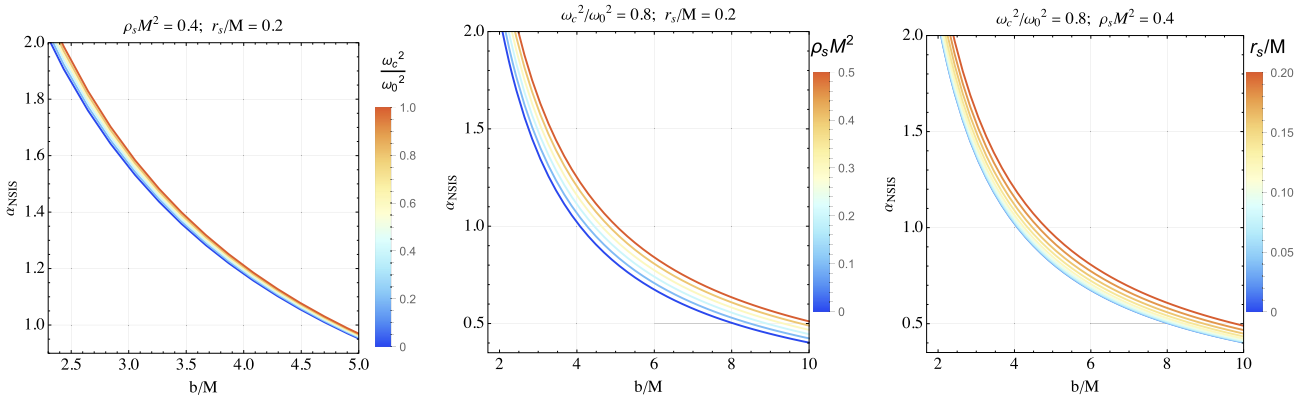


Fig. 10. (color online) Variation of $\alpha_{\rm NSIS}$ with impact parameter b, for various values of the plasma parameter ω_c^2/ω_0^2 and the dark-matter parameters ρ_s and r_s.

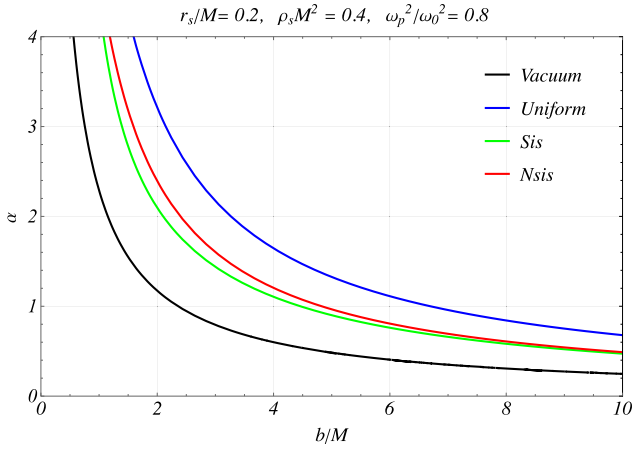


Fig. 11. (color online) Light-deflection angle α compared across models as a function of impact parameter b/M.

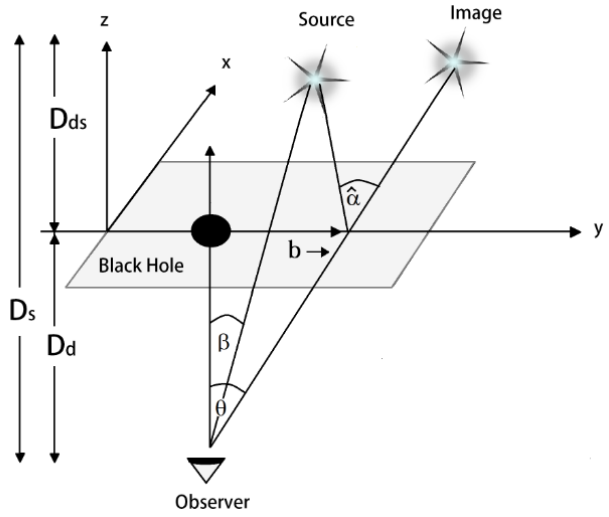


Fig. 12. Sketch of the lensing geometry: a distant source star (S) is lensed by a BH (L) and observed from Earth (O). D_d, D_s, and D_{ds} are the observer–lens, observer–source, and lens–source angular-diameter distances; β is the source's true angular position and θ the observed image position.

$$\mu_+^{\rm pl} = \frac{1}{4}\left(\frac{x}{\sqrt{x^2+4}} + \frac{\sqrt{x^2+4}}{x} + 2\right), \tag{46}$$

$$\mu_-^{\rm pl} = \frac{1}{4}\left(\frac{x}{\sqrt{x^2+4}} + \frac{\sqrt{x^2+4}}{x} - 2\right). \tag{47}$$

Summing these two contributions gives the total magnification in a uniform plasma:

$$\mu_{\rm tot}^{\rm pl} = \mu_+^{\rm pl} + \mu_-^{\rm pl} = \frac{x^2+2}{x\sqrt{x^2+4}}. \tag{48}$$

For the rest of this work, Eqs. (46)–(48), combined with the deflection angles found for the uniform-plasma and SIS profiles, allow a systematic study of how different plasma distributions affect the observed magnification of lensed sources.

A. Uniform plasma

Building on the analysis of a BH in uniform plasma, the angular positions of the lensed images can be found analytically. The dimensionless source-position parameter $x = \beta/\theta_0$ entering the magnification formulas (Eqs. 46–48) must accordingly be rescaled to reflect the plasma-modified deflection, taking the simple form

$$x = \frac{\beta/\theta_0}{\sqrt{\hat{\alpha}_{\rm uni}(\omega_e/\omega)}} = \frac{x_0}{\sqrt{\hat{\alpha}_{\rm uni}}}, \tag{49}$$

with $x_0 \equiv \beta/\theta_0$ the vacuum dimensionless source position and $\hat{\alpha}_{\rm uni} \le 1$ the frequency-dependent, normalized deflection angle in uniform plasma obtained above.

Figure 13 plots the total magnification $\mu_{\rm tot,uni}$ against ω_p^2/ω_0^2 for different King-halo parameters $\rho_s M^2$ (left) and r_s/M (right); the magnification rises markedly as the uniform plasma density increases.

B. Singular isothermal sphere

We apply the same procedure here to examine how an SIS plasma distribution affects the observed magnifications.

The angular positions of images lensed through an SIS plasma have already been worked out in the literature (see, *e.g.*, [63]), so the dimensionless source-position parameter $x = \beta/\theta_0$ needed for the magnification formulas (Eqs. 46–48) must be rescaled to reflect the SIS plasma's reduced deflection, giving

$$x = \frac{\beta/\theta_0}{\sqrt{\hat{\alpha}_{\rm SIS}(\omega_e/\omega)}} = \frac{x_0}{\sqrt{\hat{\alpha}_{\rm SIS}}}, \tag{50}$$

with $x_0 \equiv \beta/\theta_0$ the vacuum dimensionless source position and $\hat{\alpha}_{\rm SIS}(\omega_e/\omega) \le 1$ the normalized SIS deflection angle computed in Section VI.

Figure 14 plots the total SIS magnification $\mu_{\rm tot,sis}$ against ω_c^2/ω_0^2 for different halo parameters. The SIS plasma is confirmed to suppress the background source's luminosity amplification more effectively than the uniform plasma does. A higher central density $\rho_s M^2$ and a smaller core radius r_s/M again boost the total magnification, though overall lensing efficiency stays well below the vacuum value.

Figure 15 shows the ratios $\mu_{+,\rm uni}^{\rm pl}/\mu_{+,\rm uni}$ (lower curve) and $\mu_{-,\rm uni}^{\rm pl}/\mu_{-,\rm uni}$ (upper curve) for the two images in a uniform plasma, at two values of ω_p^2/ω_0^2. Both ratios stay at or above unity across the whole range of x_0 studied, so the uniform plasma enhances rather than suppresses the magnification of both images relative to vacuum. At

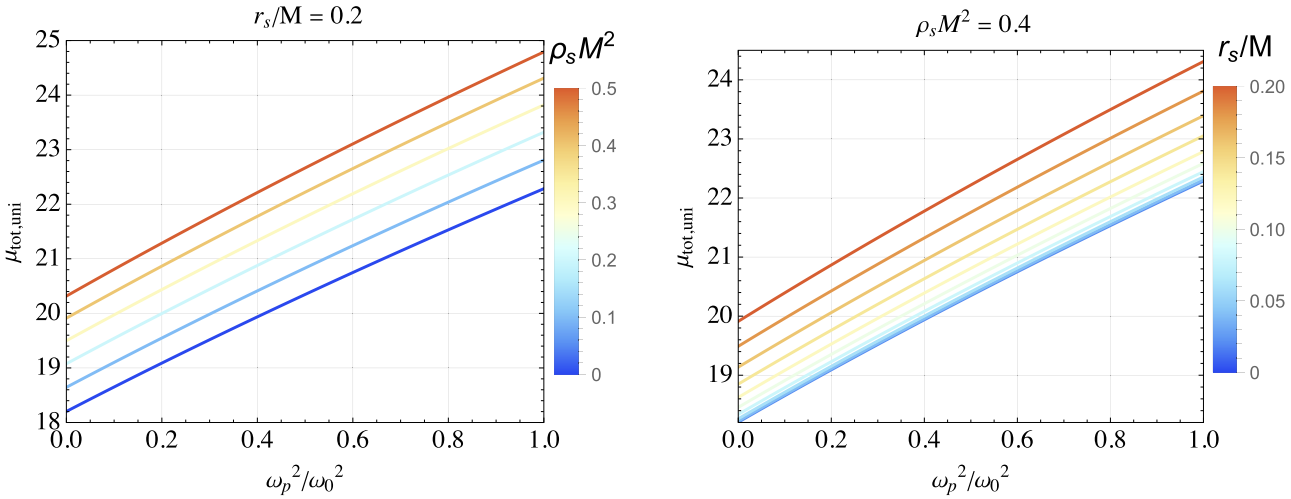


Fig. 13. (color online) Total image-brightness magnification under a uniform plasma versus ω_p^2/ω_0^2, for different dark-matter parameters ρ_s (left) and r_s (right).

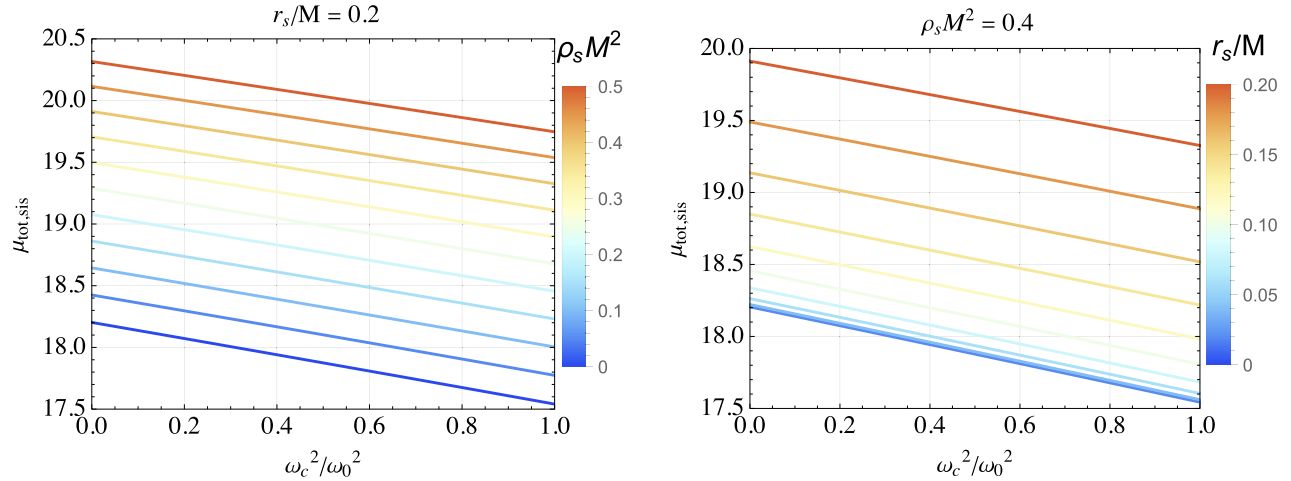


Fig. 14. (color online) Total image-brightness magnification under an SIS plasma versus ω_c^2/ω_0^2, for different dark-matter parameters ρ_s (left) and r_s (right).

small x_0 ($x_0 \lesssim 0.1$) the two ratios converge to a common value of roughly 1.4–1.5, essentially independent of ω_p^2/ω_0^2 in this regime. As x_0 grows the curves separate: the primary-image ratio (lower curve) falls monotonically toward unity for $x_0 \gtrsim 10$, while the secondary-image ratio (upper curve) rises monotonically and saturates at a value that increases with the plasma parameter, from roughly 2.15 at $\omega_p^2/\omega_0^2 = 0.5$ to roughly 2.85 at $\omega_p^2/\omega_0^2 = 0.9$. The secondary (negative-parity) image is thus always amplified more strongly by the uniform plasma than the primary image, and this gap widens as the plasma density grows.

Figure 16 shows the analogous ratios $\mu^{\rm pl}_{+,\rm sis}/\mu_{+,\rm sis}$ (lower curve) and $\mu^{\rm pl}_{-,\rm sis}/\mu_{-,\rm sis}$ (upper curve) for the SIS plasma distribution. As before, both ratios stay at or above unity across the range of x_0 shown, confirming that the SIS plasma likewise enhances rather than suppresses the magnification relative to vacuum, albeit far more weakly than the uniform plasma. The two ratios meet near 1.05 at small x_0 and diverge as x_0 grows, with the primary-image ratio falling toward unity and the secondary-image ratio climbing to a saturation value of about 1.14 ($\omega_c^2/\omega_0^2 = 0.5$) or 1.24 ($\omega_c^2/\omega_0^2 = 0.9$). This behaviour qualitatively parallels the uniform-plasma case, with the secondary image preferentially amplified, though the SIS-induced enhancement is roughly an order of magnitude smaller overall than that of the uniform plasma.

Finally, Figure 17 directly compares the magnification ratios for the uniform (solid curves) and SIS (dashed curves) models, using matching plasma-strength parameters and an identical dark-matter halo configuration. Over the plasma-frequency range studied, the SIS distribution consistently produces weaker magnification enhancement for both images than the homogeneous plasma, with the discrepancy most pronounced for the negative-parity

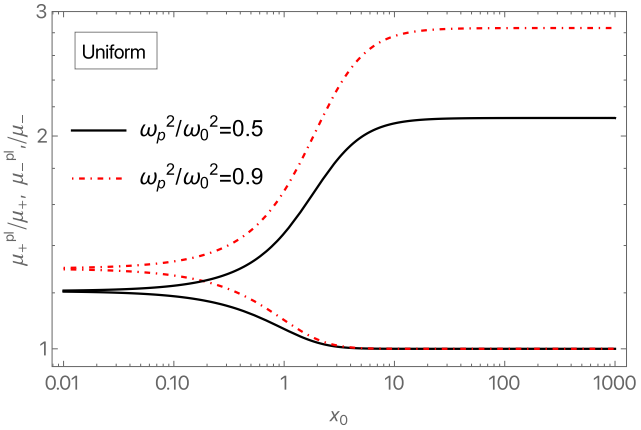


Fig. 15. (color online)Image-magnification ratios $\mu^{\rm pl}_{+,\rm uni}/\mu_{+,\rm uni}$ (lower curve) and $\mu^{\rm pl}_{-,\rm uni}/\mu_{-,\rm uni}$ (upper curve) for a uniform plasma; fixed parameters $R_s = 2M$, $b = 3M$, $\rho_s M^2 = 0.4$, $r_s/M = 0.2$.

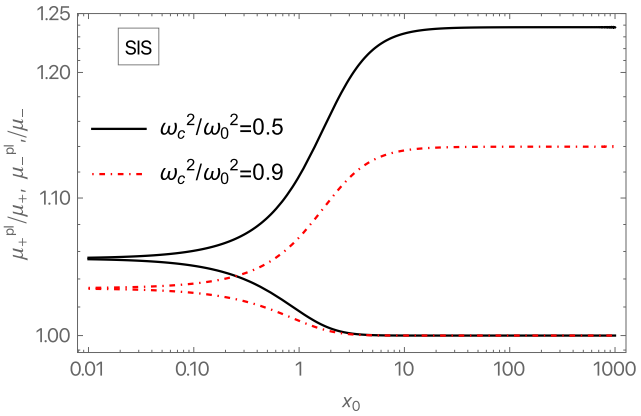


Fig. 16. (color online) Lower and upper curves give $\mu^{\rm pl}_{+,\rm SIS}/\mu_{+,\rm SIS}$ and $\mu^{\rm pl}_{-,\rm SIS}/\mu_{-,\rm SIS}$ for the image magnifications under an SIS plasma; fixed parameters $R_s = 2M$, $b = 3M$, $\rho_s M^2 = 0.4$, $r_s/M = 0.2$.

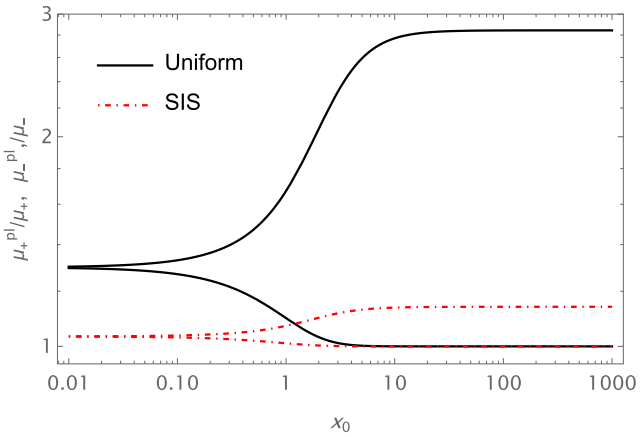


Fig. 17. (color online) $\mu^{\rm pl}_{+}/\mu_{+}$ (lower curve) and $\mu^{\rm pl}_{-}/\mu_{-}$ (upper curve) for the image magnifications under uniform and SIS plasma; fixed parameters $R_s = 2M$, $b = 3M$, $\rho_s M^2 = 0.4$, $r_s/M = 0.2$, $\omega_p^2/\omega_0^2 = 0.9$, $\omega_c^2/\omega_0^2 = 0.9$.

image, demonstrating that, at comparable plasma strength, the uniform plasma yields a substantially larger relative enhancement than the SIS plasma.

VIII. CONCLUSION

This work has presented, to our knowledge, the first comprehensive and unified theoretical treatment of the observational signatures produced by a Schwarzschild black hole set within a physically motivated King dark-matter halo and immersed in a cold, non-magnetized plasma. Deriving an exact analytic spacetime metric for the specific King profile and applying the Hamilton–Jacobi formalism for dispersive media, we have systematically computed the photon sphere, black-hole shadow, gravitational light deflection, and image magnification for both homogeneous and inhomogeneous plasma distributions.

Our main results can be summarized as follows:

1. Without dark matter, the exact metric reduces smoothly to the Schwarzschild solution. A King halo enlarges both the event-horizon and photon-sphere radii, while plasma consistently pushes the photon sphere outward relative to its vacuum position.

2. Even though the photon sphere grows larger, plasma systematically shrinks the shadow's apparent angular size. Present-day EHT observations of M87* and Sgr A* remain fully consistent with realistic King halos, imposing only very mild upper limits on the central dark-matter density; plasma introduces only a small shift in the allowed parameter space. Future EHT upgrades reaching $\sim 1\,\mu$as precision should tighten these limits considerably and may be able to separate plasma-affected models from pure-vacuum scenarios.

All three plasma models considered enhance gravitational light bending relative to vacuum, with the homogeneous plasma giving the strongest boost and the inhomogeneous SIS profile the weakest, following the clear ordering

$$\hat{\alpha}_{\rm uni} > \hat{\alpha}_{\rm NSIS} > \hat{\alpha}_{\rm SIS} > \hat{\alpha}_{\rm vac}.$$

Even modest plasma concentrations near the black hole can alter the lensing signal by factors of several at small impact parameters, with the uniform plasma producing the most pronounced departure from vacuum.

3. Both the uniform and SIS plasmas produce marked demagnification of the lensed images relative to vacuum, and the negative-parity (secondary) image is affected most severely. The SIS profile causes the strongest sup-

pression, confirming that a centrally concentrated, inhomogeneous plasma screens the lensing effect far more efficiently than a homogeneous medium of the same average density.

These findings carry meaningful implications for current and upcoming observational programs. Ignoring realistic plasma effects when interpreting strong-field (EHT) or weak-field (LSST, Roman Space Telescope, Gaia, Theia) lensing data for supermassive and intermediate-mass black holes risks mistaking ordinary plasma screening for evidence of non-standard physics, such as modified gravity, scalar fields, or alternative black-hole solutions. On the other hand, the fact that enhanced lensing signals from dense dark-matter concentrations remain detectable even amid dispersive plasma supports weak-lensing and microlensing searches as promising probes of compact, "nuclear" dark-matter halos around galactic-center black holes, as distinct from the extended galactic-scale halo.

Future work should extend the present analysis to rotating black holes within King halos, incorporate more realistic magnetized and relativistic plasma flows, and compare in detail with hydrodynamic simulations of accretion and broad-line-region plasmas around M87* and Sgr A*. Such refinements will be essential for disentangling the separate contributions of dark matter, plasma, and general relativity in next-generation black-hole imaging and astrometric measurements.

References

[1] P. Gondolo and J. Silk, Phys. Rev. Lett. **83**, 1719 (1999)
[2] M. Alloqulov, A. Abdujabbarov, B. Ahmedov *et al*., (2025), arXiv: 2512.12672[gr-qc]
[3] P. Ullio, H. Zhao, and M. Kamionkowski, Phys. Rev. D **64**, 043504 (2001)
[4] I. R. King, Astrophys. J. **71**, 64 (1966)
[5] P. H. Chavanis, M. Lemou, and F. Méhats, Phys. Rev. D **92**, 123527 (2015), arXiv: 1409.7840[astro-ph.CO]
[6] N. Blinov, S. Profumo, and T. Stefaniak, JCAP **07**, 028 (2015), arXiv: 1504.05949[hep-ph]
[7] S. N. Nuritdinov, A. A. Muminov, and F. U. Botirov, Astron. Astrophys. Trans. **32**, 83 (2021), arXiv: 2002.09310[astro-ph.GA]
[8] A. Pathrikar, (2025), arXiv: 2511.02355[gr-qc]
[9] U. Uktamov, S. Shaymatov, B. Ahmedov *et al*., Eur. Phys. J. Plus **141**, 513 (2026), arXiv: 2509.00460[gr-qc]
[10] F. Atamurotov, S. Shaymatov, P. Sheoran, and S. Siwach, JCAP **08**, 045 (2021), arXiv: 2105.02214[gr-qc]
[11] G. Crisnejo, E. Gallo, and A. Rogers, Phys. Rev. D **99**, 124001 (2019)
[12] F. Atamurotov, O. Yunusov, A. Abdujabbarov *et al*., New Astron. **105**, 102098 (2024)
[13] K. Akiyama *et al*. (Event Horizon Telescope), Astrophys. J. Lett. **910**, L13 (2021), arXiv: 2105.01173[astro-ph.HE]
[14] K. Akiyama *et al*. (Event Horizon Telescope), Astrophys. J. Lett. **930**, L12 (2022), arXiv: 2311.08680[astro-ph.HE]
[15] F. Ahmed and E. O. Silva, (2025), arXiv: 2510.16260[gr-qc]
[16] S. Jumaniyozov, Eur. Phys. J. C **85**, 1267 (2025)
[17] S. Zare, F. Hosseinifar, L. M. Nieto *et al*., (2025), arXiv: 2510.03925[gr-qc]
[18] U. Uktamov, S. Shaymatov, B. Ahmedov *et al*., Eur. Phys. J. C **85**, 1432 (2025), arXiv: 2505.20031[gr-qc]
[19] J. Sharipov, T. Xamidov, Q. Wu *et al*., (2025), arXiv: 2511.10043[gr-qc]
[20] F. Atamurotov, A. Abdujabbarov, and J. Rayimbaev, Eur. Phys. J. C **81**, 118 (2021)
[21] F. Mushtaq, X. Tiecheng, M. Yasir *et al*., Phys. Dark Univ. **50**, 102109 (2025)
[22] S. Jumaniyozov, J. Rayimbaev, M. Akhmedov *et al*., Phys. Dark Univ. **50**, 102161 (2025)
[23] M. Zahid, S. U. Khan, J. Ren *et al*., Int. J. Mod. Phys. D **31**, 2250058 (2022)
[24] K. Kobialko, D. Gal'tsov, and A. Molchanov, Phys. Rev. D **112**, 044039 (2025)
[25] S. Saydullayev, I. Nishonov, M. Dusaliyev *et al*., Eur. Phys. J. C **85**, 1081 (2025)
[26] W. Javed, R. Babar, and A. Övgün, Phys. Rev. D **100**, 104032 (2019), arXiv: 1910.11697[gr-qc]
[27] D. Umarov, F. Atamurotov, A. Abdujabbarov *et al*., (2026), arXiv: 2607.07487[gr-qc]
[28] S. Jumaniyozov, S. U. Khan, J. Rayimbaev *et al*., Phys. Rev. D **112**, 044068 (2025)
[29] F. Ahmed, S. Shaymatov, C. Yuan *et al*., (2026), arXiv: 2607.24154[gr-qc]
[30] A. Ashraf, C. Yuan, A. Bouzenada *et al*., Int. J. Geom. Methods Mod. Phys. **23**, 2650052 (2650)
[31] Z. Turakhonov, H. Hoshimov, A. Davlataliev *et al*., Nucl. Phys. B **1029**, 117566 (2026)
[32] W. Yang, M. Alloqulov, A. Abdujabbarov *et al*., (2026), arXiv: 2603.15241[gr-qc]
[33] B. Shodikulov, M. Mirov, F. Atamurotov *et al*., Phys. Dark Univ. **50**, 102096 (2025)
[34] S. Jumaniyozov, J. Rayimbaev, and Y. Turaev, Eur. Phys. J. C **85**, 1247 (2025)
[35] P. Gibbon, in *CAS - CERN Accelerator School 2019: High Gradient Wakefield Accelerators* (2020), arXiv: 2007.04783[physics.acc-ph]
[36] M. Alloqulov, Y. Isaqjonov, S. Shaymatov *et al*., Chin. Phys. C **49**, 045104 (2025)
[37] A. Alimova, Z. Turakhonov, F. Atamurotov *et al*., Phys. Dark Univ. **47**, 101749 (2025)
[38] M. M. Gohain, K. Bhuyan, and P. Chutia, Phys. Dark Univ. **49**, 102064 (2025), arXiv: 2504.00581[hep-th]
[39] F. Atamurotov, M. Jamil, and K. Jusufi, Chin. Phys. C **47**, 035106 (2023), arXiv: 2212.12949[gr-qc]
[40] G. Mustafa, O. Donmez, D. J. Gogoi *et al*., JCAP **2026**, 065 (2026), arXiv: 2602.08911[gr-qc]
[41] M. Zahid, J. Rayimbaev, F. Sarikulov *et al*., Eur. Phys. J. C **83**, 855 (2023)
[42] J. Rayimbaev, D. Bardiev, T. Mirzaev *et al*., Int. J. Mod. Phys. D **31**, 2250055 (2022)
[43] A. Chowdhuri and A. Bhattacharyya, Phys. Rev. D **104**, 064039 (2021)
[44] M. Alloqulov, S. Shaymatov, A. Jawad *et al*., Commun. Theor. Phys. **77**, 015402 (2025)

[45] A. Ashraf, O. Donmez, C. Yuan *et al*., Phys. Dark Univ. **52**, 102274 (2026)
[46] M. A. Raza, J. Rayimbaev, F. Sarikulov *et al*., Phys. Dark Univ. **44**, 101488 (2024)
[47] S. Kala and J. Singh, Eur. Phys. J. C **85**, 1047 (2025), arXiv: 2507.17280[gr-qc]
[48] M. Alloqulov, F. Atamurotov, A. Abdujabbarov *et al*., Chin. Phys. C **48**, 115116 (2024)
[49] S. Orzuev, F. Atamurotov, A. Abdujabbarov *et al*., New Astron. **105**, 102104 (2024)
[50] M. Emtir, AJMAS **8**(3), 1838 (2025)
[51] M. Yasir, F. Mushtaq, X. Tiecheng *et al*., Phys. Dark Univ. **48**, 101838 (2025)
[52] G. Crisnejo and E. Gallo, Phys. Rev. D **97**, 124016 (2018)
[53] W. Javed, I. Hussain, and A. Övgün, Eur. Phys. J. Plus **137**, 148 (2022), arXiv: 2201.09879[gr-qc]
[54] Y. Feng, A. Ditta, G. Mustafa *et al*., Nucl. Phys. B **1008**, 116713 (2024)
[55] H. Jiang, M. Alloqulov, Q. Wu *et al*., Phys. Dark Univ. **46**, 101627 (2024)
[56] G. Z. Babar, A. Z. Babar, and F. Atamurotov, Eur. Phys. J. C **80**, 761 (2020) [Erratum: Eur. Phys. J. C **82**, 403 (2022)], arXiv: 2008.05845[gr-qc]
[57] V. S. Morozova, B. J. Ahmedov, and A. A. Tursunov, Astrophys. Space Sci. **346**, 513 (2013)
[58] A. Davlataliev, B. Narzilloev, I. Hussain *et al*., Phys. Dark Univ. **42**, 101340 (2023)
[59] G. S. Bisnovatyi-Kogan and O. Y. Tsupko, Plasma Phys. Rep. **41**, 562 (2015), arXiv: 1507.08545[gr-qc]
[60] Q. Li, Y. Zhang, Z. W. Lin *et al*., Mod. Phys. Lett. A **38**, 2350025 (2023), arXiv: 2307.04444[grqc]
[61] H. Chakrabarty, A. B. Abdikamalov, A. A. Abdujabbarov *et al*., Phys. Rev. D **98**, 024022 (2018), arXiv: 1804.00461[gr-qc]
[62] G. Z. Babar, F. Atamurotov, S. Ul Islam *et al*., Phys. Rev. D **103**, 084057 (2021), arXiv: 2104.00714[gr-qc]
[63] G. Z. Babar, F. Atamurotov, and A. Z. Babar, Phys. Dark Univ. **32**, 100798 (2021), arXiv: 2103.00316[gr-qc]
[64] C. A. Benavides-Gallego, A. A. Abdujabbarov, and C. Bambi, Eur. Phys. J. C **78**, 694 (2018), arXiv: 1804.09434[gr-qc]
[65] D. Umarov, O. Yunusov, F. Atamurotov *et al*., Chin. Phys. C **49**, 055102 (2025)